Acta Biomaterialia 107 (2020) 204–217

Contents lists available at ScienceDirect

Acta Biomaterialia

journal homepage: www.elsevier.com/locate/actbio

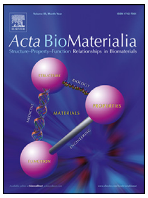

Full length article

Quantitative 3D structural analysis of the cellular microstructure of sea urchin spines (I): Methodology

Ting Yang[a,1], Ziling Wu[b,1], Hongshun Chen[a], Yunhui Zhu[b,*], Ling Li[a,*]

[a] *Department of Mechanical Engineering, Virginia Tech, Blacksburg, VA 24060, USA*
[b] *Department of Electrical and Computer Engineering, Virginia Tech, Blacksburg, VA 24060, USA*

A R T I C L E   I N F O

Article history:
Received 14 November 2019
Revised 19 February 2020
Accepted 21 February 2020
Available online 25 February 2020

Keywords:
Echinoderms
Sea urchin spines
X-ray computed tomography
3D network topology
Cellular solids
Porous structure

A B S T R A C T

The mineralized skeletons of echinoderms are characterized by their complex, open-cell porous microstructure (also known as stereom), which exhibits vast variations in pore sizes, branch morphology, and three-dimensional (3D) organization patterns among different species. Quantitative description and analysis of these cellular structures in 3D are needed in order to understand their mechanical properties and underlying design strategies. In this paper series, we present a framework for analyzing such structures based on high-resolution 3D tomography data and utilize this framework to investigate the structural designs of stereom by using the spines from the sea urchin *Heterocentrotus mamillatus* as a model system. The first paper here reports the proposed cellular network analysis framework, which consists of five major steps: synchrotron-based tomography and hierarchical convolutional neural network-based reconstruction, machine learning-based segmentation, cellular network registration, feature extraction, and data representation and analysis. This framework enables the characterization of the porous stereom structures at the individual node and branch level (~10 µm), the local cellular level (~100 µm), and the global network level (~1 mm). We define and quantify multiple structural descriptors at each level, such as node connectivity, branch length and orientation, branch profile, ring structure, etc., which allows us to investigate the cellular network construction of *H. mamillatus* spines quantitatively. The methodology reported here could be tailored to analyze other natural or engineering open-cell porous materials for a comprehensive multiscale network representation and mechanical analysis.

Statement of Significance

The mechanical robustness of the biomineralized porous structures in sea urchin spines has long been recognized. However, quantitative cellular network representation and analysis of this class of natural cellular solids are still limited in the literature. This constrains our capability to fully understand the mechanical properties and design strategies in sea urchin spines and other similar echinoderms' porous skeletal structures. Combining high-resolution tomography and computer vision-based analysis, this work presents a multiscale 3D network analysis framework, which allows for extraction, registration, and quantification of sea urchin spines' complex porous structure from the individual branch and node level to the global network level. This 3D structural analysis is relevant to a diversity of research fields, such as biomineralization, skeletal biology, biomimetics, material science, etc.

1. Introduction

Cellular materials that incorporate voids in their solid matrix are ubiquitous in nature [1]. The microstructures of natural cellular solids are diverse, including honeycombs (*e.g.*, cork and wood), closed-cell foams (*e.g.*, porcupine quill and plant parenchyma), and open-cell foams (*e.g.*, trabecular bone and echinoderm skeletons) [1]. These structures are often used for mechanics-related functions by organisms, for example, body support from bony skeletons and mechanical protection from echinoderm skeletons. These porous structures often offer high mechanical efficiency at reduced weight compared to their solid counterparts. Many classical mechanical theories for cellular solids are developed based on natural cellular materials [1,2]. Compared to synthetic ones, natural cellular materials often display rich "non-engineering" morphology features, *e.g.*, smooth transitions between branches as

---

[*] Corresponding authors.
E-mail addresses: yunhuiz@vt.edu (Y. Zhu), lingl@vt.edu (L. Li).
[1] Both the authors have equal contributions.

https://doi.org/10.1016/j.actbio.2020.02.034
1742-7061/Published by Elsevier Ltd on behalf of Acta Materialia Inc.

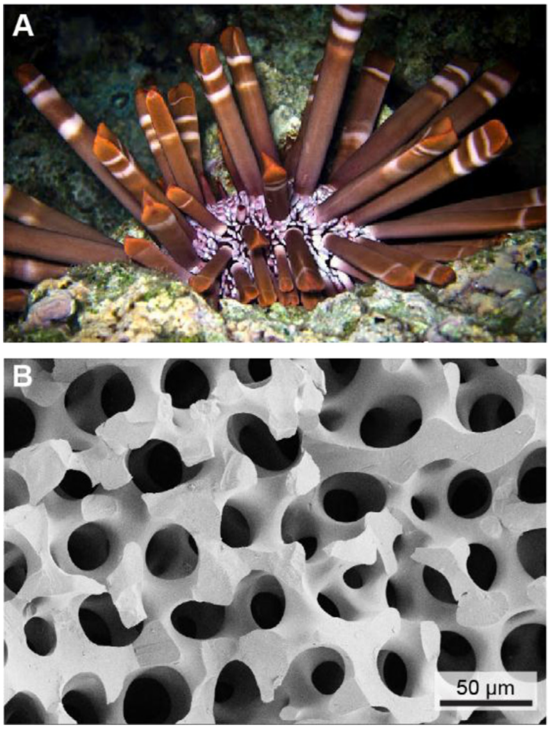

Fig. 1. The cellular structure from the spines of the sea urchin *Heterocentrotus mamillatus* used in this work. (**A**) Photograph of a live *H. mamillatus* sea urchin (Image credit, Eric Noora). (**B**) Scanning electron microscopic (SEM) image of the biomineralized cellular structure.

well as controlled structural randomness at both local and global scales [2–8]. These structural features are believed to contribute to natural cellular materials' impressive mechanical robustness, such as high stiffness, strength, and damage tolerance [4,9–12].

The skeletons of echinoderms, such as sea stars, sea urchins, sand dollars, and brittle stars, are among the most remarkable biomineralized cellular structures in nature [13]. As shown in an example from a sea urchin spine (Fig. 1), these skeletons are characterized by their complex bicontinuous porous structure, also known as stereom [14]. The stereom structures also often display controlled gradients in porosity and structural variations [5,13,14]. Remarkably, despite their complex internal microstructure, individual stereom-based skeletons are single crystals based on magnesium-bearing calcite ($((Ca_xMg_{1-x})CO_3)$) [5,15]. Although calcite is inherently weak and brittle, echinoderm skeletons exhibit high strength and excellent damage tolerance [12,16,17]. Previous studies indicated that the strength-to-weight ratio of sea urchin spines is greater than that of brick and concrete, which is attributed to the crack confining effect from the highly porous structure [7,15,18]. Such mechanical behavior contributes to the protection of echinoderms from the impact, wear, and fracture resulting from the hydrodynamic forces of waves (many echinoderms live in the intertidal zone) as well as predators [19]. Additionally, some researchers recently demonstrated that such mechanical robustness can be translated into synthetic systems, further highlighting the importance of the structural designs of echinoderms' cellular structures [5,20].

The echinoderms' stereom structures were previously examined by 2D microscopic imaging techniques [14,21–24]. Based on these studies, the stereom structures are classified into several types, such as rectilinear, laminar, galleried, labyrinthic, *etc.* [14]. Analysis of morphological variations in sea urchin spines' stereom has later been conducted by using parameters such as pore diameter and branch size [6,25]. X-ray micro-computed tomography (μ-CT) has been used for structural visualization of the stereom morphology in 3D and porosity estimation [26]. Local extracted 3D volumes were also utilized for computational mechanical modeling [9,27]. More recently, Grun and Nebelsick conducted an in-depth investigation of the stereom structure from an echinoid's plate by using a commercial tomography data analysis code [28]. This study analyzed structural parameters such as node configuration, branch length, length ratio, tortuosity, radius, orientation, and inter-branch angle for local regions [28]. Currently, we still lack a systematic methodology that allows for 3D structural quantification of stereom structures from the individual branch and node level to the global network level. This further limits our understanding of stereom's mechanical designs and the capability of developing stereom-inspired cellular material systems.

In this paper series, we present a comprehensive analysis pipeline for acquiring, processing, and analyzing the 3D cellular structures of stereom in echinoderms. By using synchrotron-based μ-CT data, this methodology allows for efficient feature recognitions of the complex cellular structures at three length scales, *i.e.*, individual node and branch level (~10 μm), local cellular level (~100 μm), and global network level (~1 mm). The structural descriptors at each level allow for an accurate and comprehensive representation and analysis of the stereom's 3D porous structure. In the first paper of this work series, we present the detailed methodology of this data analysis pipeline and demonstrate its capability with a representative volume from sea urchin spines. In the second paper, we will analyze large-volume structural variations in sea urchin spines enabled by this methodology and investigate the underlying mechanical design strategies [29].

2. Methods

2.1. Overview of the network analysis pipeline

For the 3D structural quantification of echinoderm's cellular microstructure, we combine existing and customized 3D imaging analysis algorithms into a five-step cellular network analysis pipeline based on the high-resolution tomography data (Fig. 2). This pipeline enables the high-fidelity rendition of echinoderm's complex 3D cellular microstructure with a dramatically reduced data volume (compression ratio, *ca.* 1000). This pipeline is also modular and can be further modified for network analysis of other biological or engineering open-cell porous structures. The five-step analysis pipeline is briefly summarized below:

(1) *Tomography reconstruction.* The porous microstructure from sea urchin spines is imaged with a high-resolution synchrotron-based μ-CT and subsequently reconstructed by using a Fourier grid reconstruction algorithm implemented in the open-source software TomoPy. We also developed a hierarchical convolutional neural network (CNN)-based reconstruction method, where the multiscale structural characteristics of sea urchin spines are imposed as priors during the reconstruction process to improve reconstruction quality.
(2) *Image segmentation.* The segmentation of the reconstructed *μ-CT* images is achieved through a customized machine learning method based on the training of CNN networks at multiscale length scales or using an open-source software ilastik.
(3) *Network registration.* The binarized volumetric data after segmentation is used to construct a skeletonized network structure, which is further refined through adaptive trimming and node-merging treatments. This step allows the registration of branches, nodes, and connectivity for sea urchin spines' cellular structure.

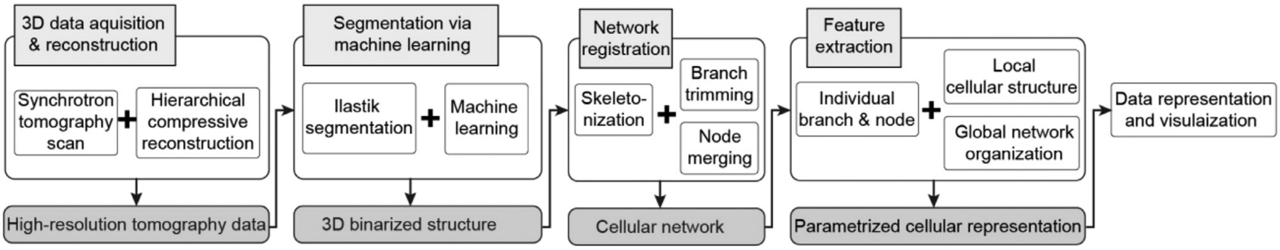

Fig. 2. Workflow of the cellular network analysis pipeline developed in this work.

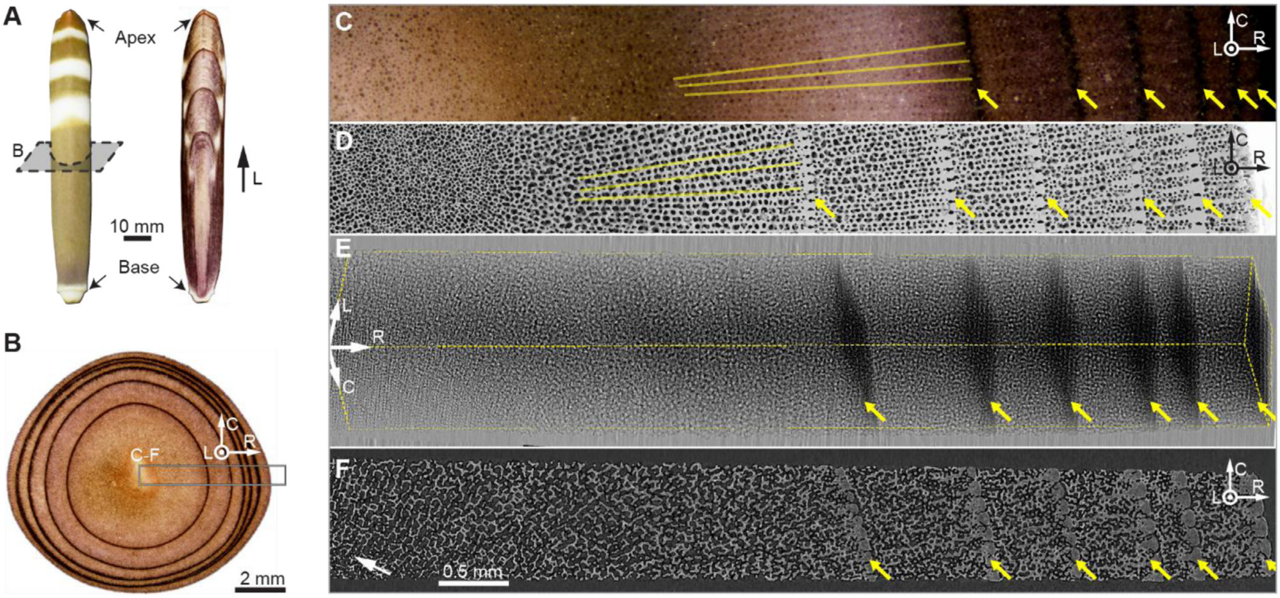

Fig. 3. Overview of the cellular structure in sea urchin spines. (**A**) The isolated individual intact *H. mamillatus* spine (left) and a spine cross section cut along the longitudinal direction (right). The longitudinal direction (L) is defined as the axial direction of the spine. (**B**) An optical image of the transversely-cut cross section of a spine, as illustrated in (**A**). A cylindrical coordinate is used in this work with two additional orientations defined: C = circumferential and R = radial directions. The dark circular lines are the growth rings. The boxed region is shown in high magnifications with different imaging techniques, including (**C**) optical image, (**D**) SEM image, (**E**) stitched projection image from synchrotron X-ray measurement, and (**F**) reconstruction image. The yellow arrows and yellow lines indicate the growth rings and septa, respectively. The white arrow indicates in (**F**) the location where the representative volumes used in this work were extracted.

(4) *Multiscale feature extraction and analysis.* The quantitative information of the registered cellular network is established at three length scales, *i.e.*, the individual branch and node level, the local cellular level, and the global network level by defining and analyzing a series of structural descriptors.

(5) *Data representation, visualization, and additional analysis.* A number of custom-written codes are developed to present and visualize the results of structural descriptors, and to convert them into data formats for additional analysis (such as finite element modeling) and visualization.

2.2. Tomography data acquisition and reconstruction

Dry spine specimens from sea urchin *H. mamillatus* (diameter, 10–15 mm) were used as a model system. A cylindrical coordinate system (L = longitudinal, C = circumferential, R = radial) was used throughout this work. A typical procedure for sample preparation and tomography measurement is summarized below (Fig. 3). Transverse sections (thickness, ~1 mm) were cut from spines by using a low-speed diamond saw (Fig 3A and B). Subsequently, a rectangular block along the radial direction was cut from the circular section (boxed area in Fig. 3B). The samples were then imaged via synchrotron-based µ-CT measurements at the beamline 2-BM at Advanced Photon Source, Argonne National Laboratory. A monochromatic beam with an energy of 27.4 keV was used. Each tomography scan consisted of 1500 projection images for a 180-degree rotation with a rotation speed of 0.5°/second. The projection images were collected by using a PCO Edge highspeed CMOS detector (2560 × 2160 pixels). The system was equipped with a 10x long-working-distance objective lens, which resulted in an isotropic voxel size of 0.65 µm. This ensures enough resolution for analyzing the local branch morphology with at least 10 voxels sampled across branch cross sections. For larger samples, we extended the field of view by collecting multiple scans with ~90 µm overlaps and then stitching them using Fiji/ImageJ [30]. A stitched projection image and a corresponding longitudinal view of the reconstruction slice are shown in Fig. 3E and F, respectively. Corresponding optical and scanning electron microscopy (SEM) images in the same orientation are shown in Fig. 3C and D. Representative volumes close to the spine center (indicated by the white arrow, Fig. 3F) were selected in this work to develop and demonstrate the capability of the analysis methodology.

The tomographic reconstruction of the collected projection images is achieved through two methods: a standard Fourier grid reconstruction algorithm implemented in TomoPy [31,32] and a custom-developed hierarchical CNN method [33]. For both methods, the CT imaging process is modeled as the Radon transform R, where the projection measurement (also known as sinogram) g is obtained through the integral along each projection line l of the object function $f(r)$ as

$$g(s,\theta) = R[f(\mathbf{r})] = \int_{\{\mathbf{l}:\ \mathbf{r}\cdot\theta\ =\ s\}} f(\mathbf{r})\ d\mathbf{r} \qquad (1)$$

where θ is the projection angle, s denotes the position on the detector, $f(\boldsymbol{r})$ represents the X-ray linear attenuation coefficients at different voxels of the object. A CT reconstruction problem is formulated as retrieving the unknown function $f(r)$ based on the observed sinogram $g(s,\ \theta)$. TomoPy provides an analytical reconstruction method based on the Fourier grid reconstruction algorithm [31]. The reconstruction artifacts and noises associated with this reconstruction are suppressed by removing abnormal pixels and stripes from the sinogram $g(s,\ \theta)$ before reconstruction [34,35]. To minimize the diffraction-induced blurring at the sharp interfaces in the porous stereom, a phase retrieval step is conducted to sharpen the boundaries of the reconstructed objects [36–40] . Desired sharpness of edges is obtained by manually tuning the relative strength between the absorption and the phase diffraction (Fig. S1A and B).

Instead of manually tuning parameters analytically, the hierarchical CNN reconstruction algorithm relies on a data-training process to separate the artifacts and noises from the structure. Due to the adaption to the targeted dataset, this method can greatly increase reconstruction efficiency. We have noticed that the porous spine specimens display structural features on three different length scales including

1. at the individual voxel level, each voxel is categorized into one of the two phases, *i.e.*, solid from the branches and nodes, void from the pores. The boundary between these two phases is clear and smooth;
2. at the local cellular level, the branches and nodes are formed with similar shapes. The structure is bicontinuous, which means each phase is interconnected without the presence of isolated elements, *i.e.*, isolated solid particles or completely embedded holes. Moreover, the branches within a local region (~100 μm) are characterized by a similar thickness and length;
3. and at the long-range network level, the arrangements of branches and nodes are uniform and semi-periodic.

The hierarchical CNN architecture allows us to learn the structural characteristics of stereom at these three length scales, respectively. This is achieved by filtering the reconstruction images through three different spatial frequency filters and training individual CNNs on each scale, respectively. These learned structural characteristics δ_i are imposed as priors during the reconstruction process, which is implemented by formalizing a constraint optimization problem by

$$\hat{f} = \underset{x}{\operatorname{argmin}} \frac{1}{2}||Rf - g||_2^2 + \sum \lambda_i \|\delta_i(f)\|^2 \tag{2}$$

Here the first term represents the fidelity term (fitness), which contains the difference between the object $f(r)$ and the sinograms $g(s,\ \theta)$. The second term is the regularization term that describes the structural priors. These learned structures are then combined to generate the full-scale μ-CT reconstruction that suppresses noises and artifacts. This method allows for high-fidelity reconstruction with reduced projection images and exposure time. The reconstruction based on TomoPy with 75 projections exhibits severe noises and artifacts in the background (Fig. S1C). In contrast, our reconstruction method can achieve comparable reconstruction based on 75 projections with that from the TomoPy method with 1500 projections (Fig. S1D). In order to demonstrate the capability of the cellular network analysis algorithm, all the results reported in this work are based on the reconstructions by using the standard TomoPy method.

2.3. Image segmentation

Two approaches were utilized to segment the reconstruction data for further cellular network analysis. The first approach was based on the open-source software, ilastik [41]. A customized machine learning-based segmentation method was also developed to reduce segmentation artifacts using a data-driven learning process. In this method, we first generated the training dataset, consisting of the reconstruction slices with manually labeled segmentation. An image translation CNN is trained on the training dataset, which produces segmentation estimates for future input of reconstruction slices. Similar to the hierarchical reconstruction algorithm, we focused on the three featured length-scales of the sea urchin spines during the training process. This method yields comparable results with the segmentation results from ilastik, but with much reduced manual work (Fig. S2). This hierarchical CNN approach proved to be robust in reducing various noises and artifacts in our μ-CT reconstructions [42]. In this paper, our cellular network analysis is based on the segmentation results from ilastik, following the same argument regarding the reconstruction step.

2.4. Network construction and registration

The segmented volumetric data was used as the input for the cellular network analysis followed by the procedures below.

Skeletonization: A custom-written 3D thinning algorithm based on an iterative erosion method was developed to extract the 3D skeleton of the cellular structure from the binarized data, which represents individual branch as a line with one voxel thickness [43,44] (Fig. 4A-C). The skeleton of the cellular structure consists of a network of branches interconnected with nodes. The node of the skeleton is defined as the voxel with more than two neighbor voxels. The position of the node is also used to register individual branches by specifying the starting and ending nodes. The network after the direct skeletonization treatment suffers from several inherent artifacts, including extrusions from dangling branches (Fig. 4E) and node clusters characterized by unrealistic short branches, which will be addressed in the following steps (Fig. 4F). The current skeletonization method works well with sea urchin spine's porous structures consisting of rod-like branches; however, for porous structures with "plate-like" morphologies as in some trabecular bone, further improvement of the algorithm is required.

Adaptive trimming: To refine the skeletonized network, we applied an adaptive trimming process to remove extruded branches that are not connected to the network at one end (Fig. 4E). These extruded or dangling branches may be due to the local surface variation of the cellular structure. In addition, branches that are cut off by the volume boundaries also exhibit as extruded branches (red arrows, Fig. 4C). Extruded branches are identified by inspecting the connectivity and lengths of branches within the analyzed network. As the side effect of this removal step, nodes connected by two branches, which are referred to as N-2 nodes, emerge. We identified each pair of branches connected by these N-2 nodes and connected these branch pairs by replacing these N-2 nodes with branch points. The connectivity of the network is updated after each trimming step until all the extruded branches are removed, as shown in an example in Fig. 4G.

Node merging: After removing the extruded branches with the adaptive trimming, further refinement was conducted on nodes. The node cluster that is composed of nodes connected with very short branches is considered as artifacts of skeletonization (Fig. 4F). We first dealt with one special case of node cluster, *i.e.*, adjacent nodes that are directly connected without branch points between the nodes. Connected nodes are results from the skeletonization of the non-smooth discrete volume, where extrusions are recognized as branches with unnecessary nodes. We replaced connected nodes with one single node, the coordinate of which is in the center of the node cluster. The connectivity of the network is updated after this merging procedure. For the general case of node clusters, we removed short branches and merged the node cluster into one

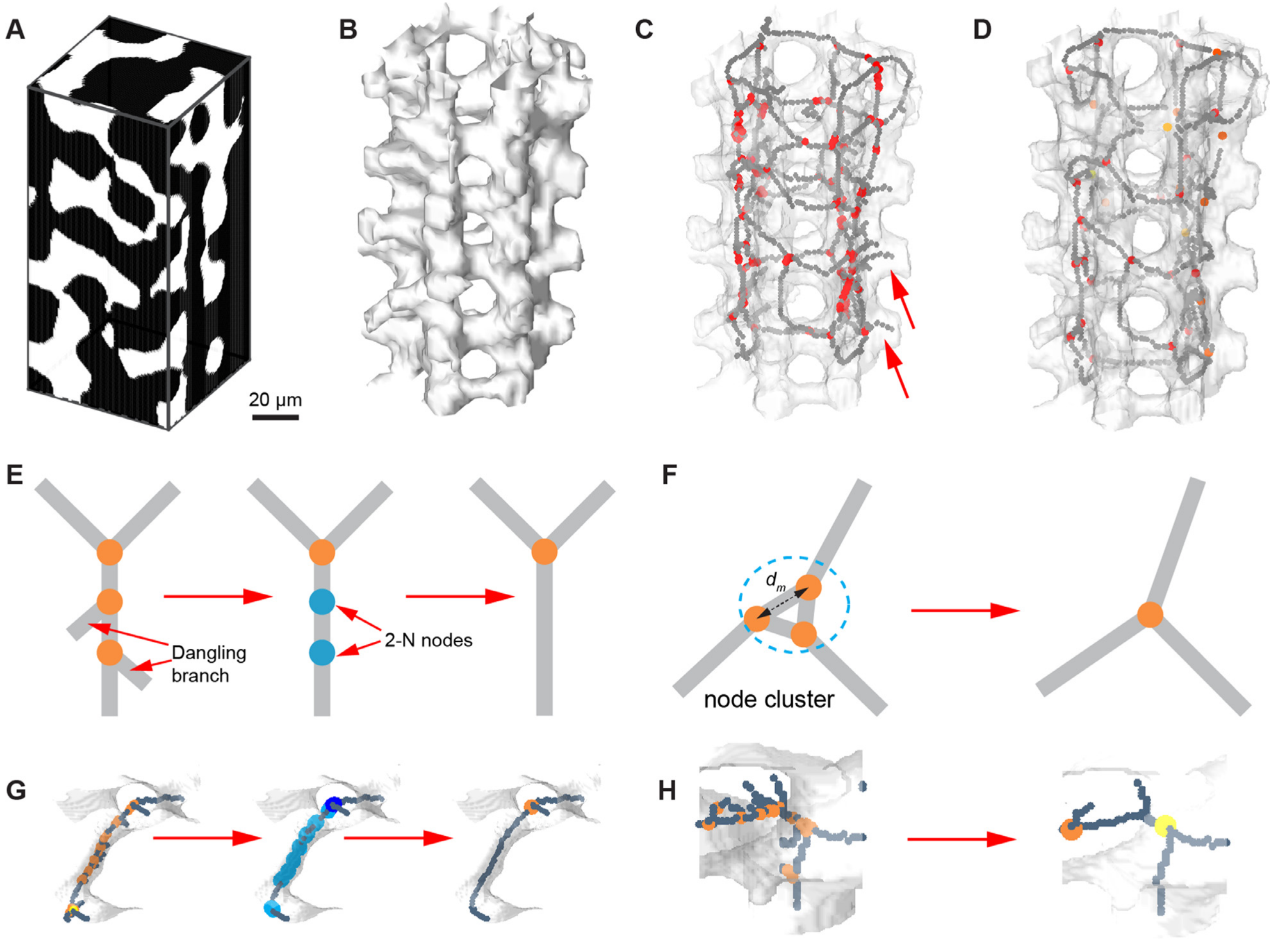

Fig. 4. Network construction. (**A**) A representative volume based on the segmented binary data. (**B**) 3D rendering of the cellular structure, and corresponding (**C**) cellular network consisted of branches (gray lines) and nodes (red dots) after initial skeletonization and (**D**) after adaptive trimming and node merging. (**E**) Schematic illustration and (**G**) a corresponding representative example of the adaptive trimming process, which removes extruded dangling branches and associated nodes. (**F**) Schematic illustration and (**H**) a corresponding representative example of the node merging process, through which node clusters with distances between adjacent nodes smaller than a critical distance, d_m, will be merged to a single node.

node in the center of the cluster. In our analysis, we set the threshold of merging distance $d_m = 10$ voxels (= 6.5 µm) to be roughly the mean branch radius (6.2 µm). As shown by a typical example in Fig. 4H, many node clusters are present in the original skeletonized network, and this merging process is critical to clean the unnecessary nodes and short branches.

The aforementioned steps establish the cellular network of the original tomography data of the sea urchin spine's porous structure. The network information, including nodes, branches, and their associated surface profiles, is registered in terms of a weighted graph $G = \{N, B, P\}$, where N and B represent for the nodes and the branches, respectively. The associated surface profiles, P, for individual branches are registered by using the binarized volumetric data. This allows for further structural quantification, such as branch thickness, surface curvature, and node diameter. The size of this combined network representation is 0.1% of the original tomography data, yet it carries the essential geometric information of the original structure.

2.5. Feature extraction and analysis

In this step, we developed an automatic computer vision-based pipeline to extract, classify, and analyze the structural descriptors of the registered cellular network and surface morphology at three length scales, namely, the individual node and branch level, the local cellular level, and the global network level (Fig. 5).

Individual node and branch level: The network connectivity registration identifies individual branch, B_{ij}, which is bounded with two end nodes, N_i and N_j, as shown in Fig. 5A-i. The branch length is calculated with two metrics, the Euclidean distance, l_{ij}, defined as the straight distance between the starting and ending nodes, and the physical branch length, $l_{o,\ ij}$, obtained by accumulating the distances in all neighboring voxels on the branch. The physical length $l_{o,\ ij}$ records the curviness of the branch and therefore is usually greater than the Euclidean distance l_{ij}. We define the branch length ratio as $s_{ij} = l_{o,\ ij}/l_{ij}$. The branch orientation is characterized by two angles, the misorientation angle, θ, and the in-plane rotation angle, ω. θ is defined as the angle between the branch vector and a reference global direction (*e.g.*, the L direction). For calculation of the in-plane rotation angle ω, the branch vector is first projected to the plane perpendicular to the defined global direction (*e.g.*, the R-C plane for the L direction). ω is then defined as the angle between the projection direction and another selected in-plane reference direction (*e.g.*, the R direction). The in-plane misorientation angle ω ranges from 0° to 360°.

The branch profile, $P_{ij}(l)$, is used to describe the cross-sectional size and morphology along the length of each branch (Fig. 5A-i). This is achieved by registering the intersecting line profiles between the cross-sectional planes (perpendicular to B_{ij} at the sampling point) and branch surface at a given location of l. This allows for the determining the branch profile, P_{ij}, by using the radius of an equivalent circle with the same area of the intersecting

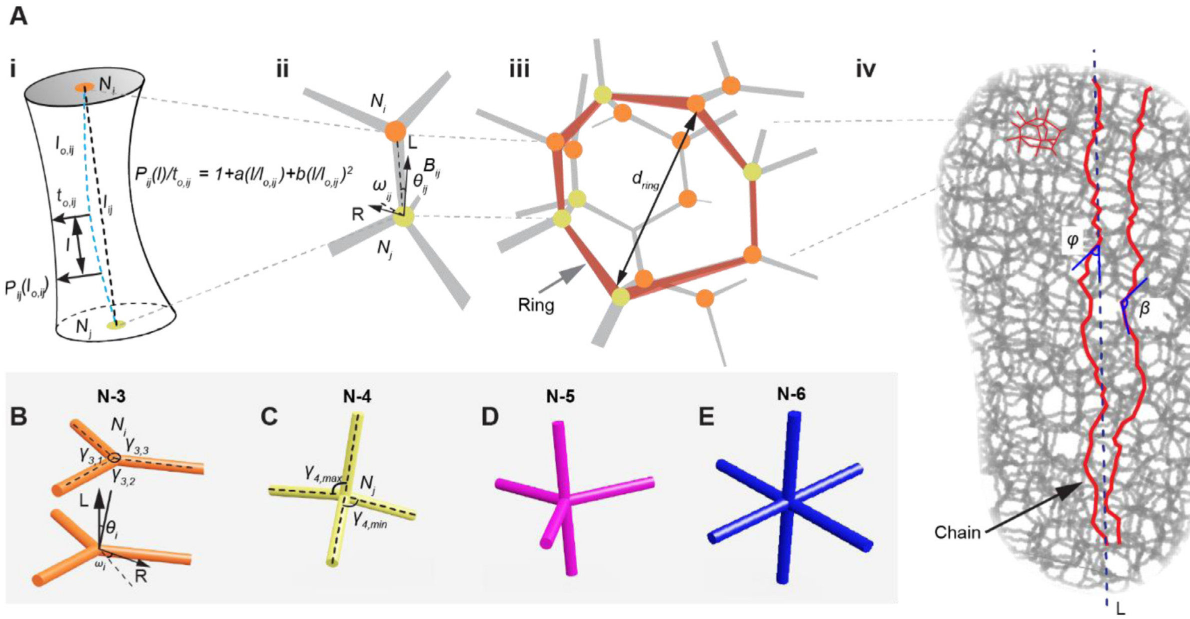

Fig. 5. A multiscale representation scheme for the cellular network of sea urchin porous structures. (**A**) On the individual branch and node level (panel i and ii), each branch is denoted as B_{ij} bounded by two nodes N_i and N_j. The branch is characterized by its length ($l_{o,\,ij}$), Euclidean distance (l_{ij}), orientation (θ_{ij} and ω_{ij}), thickness ($t_{o,\,ij}$) and morphology profile $P_{ij}(l)$. θ_{ij} is the misorientation angle of the branch from the L direction. ω_{ij} denotes the angle between the branch projection and the R direction in the R-C plane. The branch morphology along a branch is captured and fitted into a quadratic function ($P_{ij}(l)$). On the local cellular level (panel iii), the node types (represented by colored dots) and ring structures formed by connected branches (highlighted in red) are registered. The ring diameter is denoted as d_{ring}. On the global network level (panel iv), the long-range alignment of branches, denoted as "branch chain", can be identified. Two angles are defined: φ, misorientation angle of a branch in the chain from the L direction, β, the inter-branch angle between two adjacent branches in the chain. (**B-E**) Schematic diagrams of idealized N-3, −4, −5, and −6 nodes. $\gamma_{3,\,1}, \gamma_{3,\,2}, \gamma_{3,\,3}$ represent the three inter-branch angles in N-3 nodes ($\gamma_{3,\,1} < \gamma_{3,\,2} < \gamma_{3,\,3}$). Mean angle $\gamma_3 = (\gamma_{3,1} + \gamma_{3,2} + \gamma_{3,3})/3$. The misorientation angle (θ) for a N-3 node is the angle between the L direction and the normal direction of the node's basal plane. By projecting this normal direction to the R-C plane, the angle ω denotes the angle between the projection and the R direction. $\gamma_{4,\,min}, \gamma_{4,\,max}$ represent the minimum and maximum inter-branch angle for N-4 nodes.

profile. The thickness in the middle of a branch is denoted as branch thickness, $t_{o,\,ij}$. The local branch thickness profile P_{ij} is fitted with a second-order polynomial

$$P_{ij}(l)/t_{o,ij} = 1 + a\left(l/l_{o,ij}\right) + b\left(l/l_{o,ij}\right)^2, \tag{3}$$

where a and b are fitting parameters.

Following the previous work on the inter-trabecular angle measurement method developed by Reznikov et al. for the analysis of trabecular bone [4,45], we quantified the node connectivity and characteristics of the cellular structure of sea urchin spines (Fig. 5A-ii). First, the node type is categorized by the number of branches connected to a given node as N-3 (with three connecting branches), N-4 (with four connecting branches), ..., and N-n (with n connecting branches) (Fig. 5B-E). The inter-branch angle for different node types is defined following the similar approach described in [4,45]. For example, for N-3 nodes, the three inter-branch angles are denoted as $\gamma_{3,\,k}$, where k(1, 2, and 3) indicates the three angles in ascending order (Fig. 5B). The average inter-branch angle for a N-3 node is denoted as γ_3. Similarly, the inter-branch angles for N-4 nodes are represented by $\gamma_{4,\text{ min}}$, γ_4, $\gamma_{4,\text{ max}}$ representing the minimum, average and maximum values (Fig. 5C).

To analyze the orientation of N-3 nodes, we defined a central axis as the node orientation that shared the same angle with each individual branch of a N-3 node (Fig. 5B). The misorientation angle θ and the in-plane rotation angle ω are defined in a similar way for the branch orientation. The direction of the central axis is selected so that the angle between the central axis and each branch is less than 90°. Due to this convention, the misorientation angle θ ranges from 0° to 180°, which is different from the θ range of branch orientations. Following the previous work on the trabecular bone [4,45], we defined the cosine of the angle between the central axis and each branch as the planarity index, which varies between 0 and 1. The plane formed by N-3 nodes is flatter when the planarity index is closer to 0.

Local cellular level: In this scale, we investigated the local interconnection characteristics of adjacent branches. An algorithm was developed to quantify the number of branches required to form a complete ring structure (Fig. 5A-iii). Briefly, the analysis process is as following: starting from a given node, a "tree-shape" structure is constructed by identifying the neighboring nodes that are connected to the starting node. As this process continues to expand the "tree" structure, a ring is identified when the original node is included in the new layer of connections. This indicates that the node is connected back to itself in a non-repeated manner. The number of branches included in a complete ring is then used to define the ring type. For instance, a 5-B ring refers to a ring composed of 5 branches. We calculated the area enclosed by the ring and fitted it into a circle. The diameter of the fitted circle is defined as the ring size (d_{ring}). All branch points that form a ring are fitted into a plane, the normal direction of which is defined as the ring direction. The ring orientation is characterized by following the same definition of branch orientation and N-3 node orientation.

Global network level: The alignment of connecting branches over a long distance is investigated by defining a branch alignment factor as $CAF_{ij}^k = \max \prod_{k=i,i+1\ldots}(c_k \cdot c_{k+1})\beta_{k,k+1}$, where c_k is the unit vector of normal direction of the k_{th} branch in a "chain" structure starting from the branch of interest. By including the inter-branch angle $\beta_{k,k+1}$ between two neighboring branches in the chain structure, *CAF* measures the degree of alignment for the most aligned k-node chain structure (Fig. 5A-iv). An iterative algorithm is implemented to detect aligned chain structure with minimized *CAF*. The quantification of inter-branch angle β, length and thickness for branches in the detected chains, and offset angle φ (the angle away from a defined global direction) is performed to evaluate the structural characteristics of these chains.

We further proposed to quantitatively describe the structural ordering at the global scale by conducting the long-range 3D fast Fourier transform (3D-FFT) analysis of the structural descriptors extracted from the full-volume registered network. In particular, we applied Fourier analysis on registered node positions over large volumes ($>$0.1 mm^3) to investigate its long-range periodicity. Note that directly implementing a Fourier analysis on the original 3D tomography data with such large volume is computationally expensive, and not necessarily informative due to the mixing of structure information on all different scales. The 3D-FFT analysis based on the node distribution resolves these challenges and provides a clear representation of the global orderliness or randomness of the cellular network.

2.6. Data presentation, visualization and additional analysis

A variety of data representation schemes were developed with custom-written MATLAB scripts to interrogate the results of cellular network analysis. These include (1) distribution of individual descriptors, (2) polar plots for orientation-dependent correlative analysis among multiple descriptors, and (3) direct representation of descriptors within the 3D skeletonized cellular network. We also developed several 3D visualization strategies of the analyzed cellular network: (1) selected descriptors (such as branch thickness, length, or node connectivity, *etc*.) are presented with a color scale in the 3D skeletonized cellular network in MATLAB directly. The binarized original tomography data can also be imported simultaneously to interrogate the cellular network results. (2) Similar results can be achieved by generating image stacks with selected descriptors (*e.g.* N-3 nodes or $l_{o,\,ij} > a$ critical value) and imported into and visualized with a commercial tomography analysis software *Avizo* (Avizo 9.5, Thermo Fisher Scientific, USA).(3) Beam models can be generated using a customized Python script to join intersecting beams based on the branch connectivity and assign thickness for each branch individually. The third visualization scheme also enabled us to conduct systematic mechanical modeling on the cellular network by using a commercial finite element analysis software *Abaqus* (Abaqus 2016, Simulia, USA), which will be discussed in the following paper of this work series.

2.7. Implementation and accessibility

The customized cellular network analysis algorithm has been implemented in MATLAB. It is available for download at https://github.com/Ziling-Wu/Quantitative-3D-structural-analysis-of-the-cellular-microstructures.

2.8. Statistical analysis

All measurements of structural descriptors are expressed as the mean ± standard deviations (SD) with sample sizes whenever possible.

3. Results

In this work, we chose the spines from sea urchin *H. mamillatus* as our model system. The *H. mamillatus* spines exhibit a gradient porous microstructure, where the porosity gradually reduces from 80 vol% in the center to 60 vol% in the edge region [26]. However, the detailed network organization of this structure in both local and global scales still remains elusive. In the current paper of this work series, we used a small region ($200\,\mu m(R) \times 250\,\mu m(C) \times 250\,\mu m(L)$) of the *H. mamillatus* spines to demonstrate the capability of our cellular network analysis method. In the second paper, we will utilize this approach to conduct a systematic characterization and analysis over a large volume to investigate the structural design strategies of this structure (Fig. 3E) [29]. The representative volumes used in this work were extracted close to the center region of a spine (Fig. 3F).

3.1. Results of network registration

The representative volume after segmentation is shown in Fig. 6A. After the initial skeletonization, this volume contains 6342 nodes and 4574 branches. The trimming process reduces the numbers to 5126 nodes and 3584 branches, and the final merging treatment further refines to 1249 nodes and 2233 branches. This significant reduction in numbers also indicates the importance of our iterative trimming and node merging process. The density of nodes and branches are ~124,900mm^{-3} and 223,300mm^{-3}, respectively. Fig. 6B shows the final registered network with the nodes and connected branches highlighted as red dots and gray lines, respectively.

3.2. Node characteristics

Due to the incomplete branches at volume boundaries, nodes ($N = 289$) and branches ($N = 1030$) within $20\,\mu m$ from the boundaries are not considered in our further analysis. Within this volume, N-3 and N-4 nodes are dominating node types (50% and 35%, respectively) (Fig. 6C and D). N-5 and N-6 nodes comprise 12% and 3%, respectively, where no N-7 and higher-branched nodes are detected. The relative frequencies of N-3: N-4: N-5: N-6 nodes are approximately 17: 12: 4: 1. Different types of nodes are uniformly distributed within this volume (Fig. 6C).

As the N-3 and N-4 nodes comprised the majority of all nodes, we further analyzed their inter-branch angles and node orientations. As shown in Fig. 6E, the smallest, median, and largest inter-branch angle for N-3 nodes are $115.5^\circ \pm 20.3^\circ$, $119.4^\circ \pm 19.1^\circ$, and $119.4^\circ \pm 18.4^\circ$, respectively. The mean value of all inter-branch angles for N-3 nodes is $118.1^\circ \pm 3.5^\circ$ ($N = 447$) with the most frequent value of 120° The measurement result is close to the ideal three-branched node with 120° as the ideal inter-branch angle, which indicates that the three branches for a N-3 node in sea urchin spines are generally evenly orientated to span as much as possible in space.

The orientations of N-3 nodes are presented in a polar distribution plot by using the misorientation angle θ and in-plane rotation angle ω. As shown in Fig. 6F, most of the N-3 nodes are oriented perpendicular to the L direction as they cluster around a circle with $\theta = 90^\circ$ In contrast, the distribution of ω is rather uniform between 0 and 360°, indicating a random distribution in the R-C plane. Fig. 6G shows the planarity index distribution of N-3 nodes. As introduced earlier, the planarity index describes the flatness of the plane formed by the N-3 nodes. 90% of the N-3 nodes have their planarity index less than 0.17, which is within 10° offset from the ideal plane; about 95% of the N-3 nodes have their planarity index less than 0.27 (corresponding to 16° offset). This indicates that the branches in N-3 nodes are roughly oriented in the same plane, consistent with the inter-branch angle measurement results.

For N-4 nodes, the smallest and largest inter-branch angles are $85.9^\circ \pm 13.6^\circ$ and $134.7^\circ \pm 16.7^\circ$, respectively, with a mean inter-branch angle of $110.0^\circ \pm 9.4^\circ$ ($N = 335$) (Fig. 6H). This result approaches the ideal tetrahedral angle of 109.5°, which indicates that

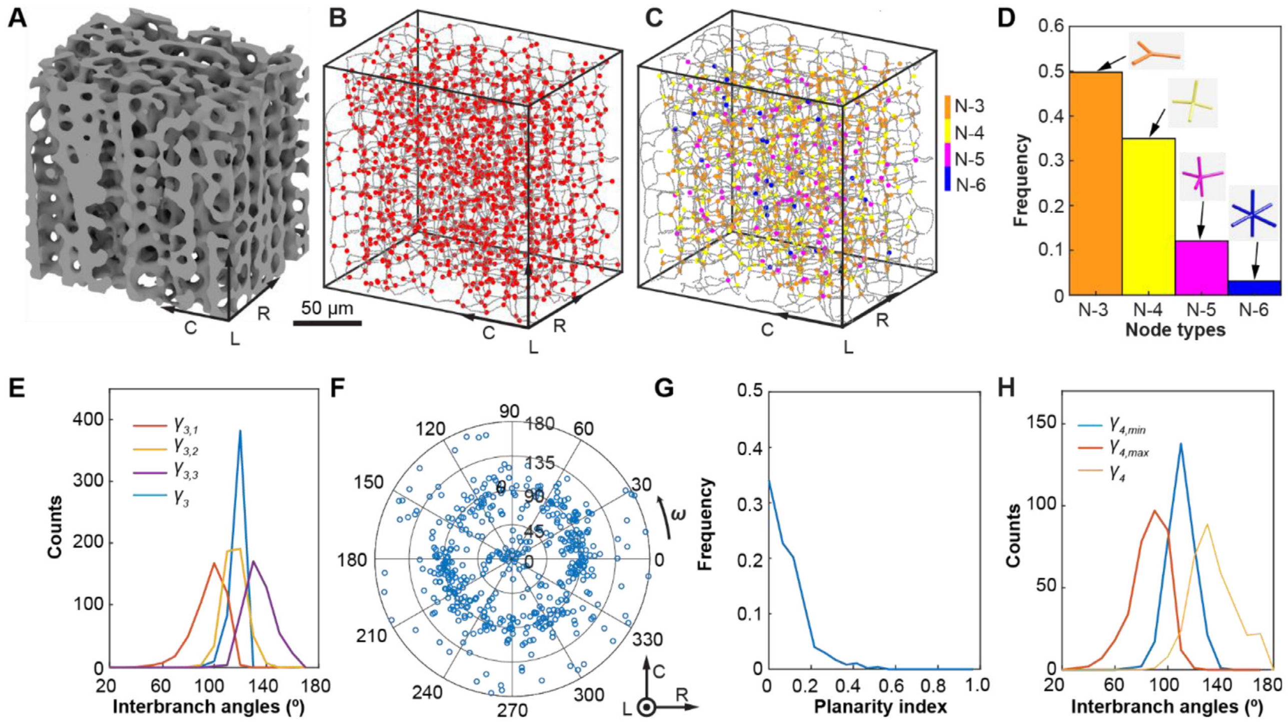

Fig. 6. Quantitative analysis of nodes. (**A**) 3D rendering and (**B**) corresponding skeletonized network of the analyzed volume close to the center region of an *H. mamillatus* spine. (**C**) Skeletonized network with node types indicated with colored dots. (**D**) Distribution of node types in this volume. (**E**) Distribution of individual ($\gamma_{3,1} < \gamma_{3,2} < \gamma_{3,3}$) and mean ($\gamma_3 = (\gamma_{3,1} + \gamma_{3,2} + \gamma_{3,3})/3$) inter-branch angles for N-3 nodes. (**F**) Orientations of N-3 nodes. (**G**) Planarity index distribution of N-3 nodes. (**H**) Distribution of inter-branch angles for N-4 nodes ($\gamma_{4,\,min}$, $\gamma_{4,\,max}$, and mean value γ_4).

the branches connected to a N-4 node also tend to maximally span the space.

3.3. Branch characteristics

As shown in Fig. 7A, the branches in the sea urchin spines' stereom structure are characterized by curved surfaces. The registered skeleton network allows us to quantify the branch length, thickness and morphology reliably. First, the physical branch length $l_{o,\,ij}$ and the Euclidean distance l_{ij} are calculated, and their distributions are shown in Fig. 7B. The mean physical length and Euclidean distance are $21.7 \pm 7.9\,\mu m$ and $18.0 \pm 6.2\ \mu m$ ($N = 1203$), respectively. The length ratio s_{ij} is 1.2 ± 0.1, indicating that most of the branches slightly deviate from straight connections (Fig. 7C). The branch length can be color mapped on the skeletonized cellular network (Fig. 7D). Short ($< 15.0\,\mu m$) and long branches ($> 40.0\,\mu m$) are further extracted and displayed in Fig. 7E and F, respectively. These 3D representations reveal that short branches are distributed evenly in the volume, whereas the long branches are oriented in the *R-C* plane. Examples of these long branches are shown in Fig. 7G and H, which confirms the preferred orientation in the *R-C* plane. The correlation between branch orientation and length can be further visualized by using the polar scatter plot (Fig. 7I). The long branches (cyan and yellow data points) typically have $\theta = 90^\circ$, indicating that they are orientated in the *R-C* plane. Moreover, the shorter branches corresponding to the blue data points exhibit a clear orientational alignment along the *L* direction with misorientation angles centered around ~20°. In addition, the uniform distribution of in-plane rotation angles ω shows no orientation preference in the *R-C* plane. These results are consistent with the direct visualization shown in Fig. 7E and F.

The calculated branch thickness t_o is shown in a colored 3D diagram mapped on the cellular network (Fig. 8A). The mean branch thickness is $6.2 \pm 1.5\,\mu m$ ($N = 1203$), and most of the branch thicknesses range from 4 to 8 μm (Fig. 8B). In addition, as shown in the polar plot of the branch thickness as a function of their orientation distributions, the thicker branches (red and yellow data points) concentrate in the center of the plot (Fig. 8C). This concentration suggests that the branches aligned in the *L* direction tend to be thicker, whereas the branches with θ values close to 90° typically have the thickness smaller than 5 μm (blue data points). Therefore, the thinner branches are mostly oriented in the *R-C* plane, which is consistent with the direct observation of the distribution of branches with $t_o < 3.3\,\mu m$ (Fig. 8D). In addition, the similarity between Fig. 8D and 7F leads us to further evaluate the correlation between the branch thickness and length. A negative correlation between the two parameters is found ($t_o = -0.14 l_o + 8.14,\ R^2 = 0.39$, Fig. 8E). This result is consistent with the observations of some long ($>40.0\,\mu m$) and thin ($<3.3\ \mu m$) branches as demonstrated in Fig. 7G and H.

In addition to the single branch thickness value at the branch middle point, the entire cross-sectional profile of each branch can be extracted as P_{ij} and then fitted with a 2nd order polynomial according to Eq. (3) (Fig. 8F). To study the general morphology characteristics of all branches, we normalized each individual branch profile with its own length l_o and thickness t_o. The fitting result is $P(l)/t_o = 1 - 0.026(l/l_o) + 1.23(l/l_o)^2$ ($R^2 = 0.899$, Fig. 8G). With previously measured $l_o = 22\ \mu m$ and $t_o = 6.2\ \mu m$, this fitted profile represents the branch morphology well, as shown in a 3D rendering of a typical branch in the volume (Fig. 8H). This finding indicates that the branch morphology in the sea urchin spines' stereom is highly curved. In addition, the cross-sectional profiles of branches in stereom may be slightly non-circular (Fig. 8H). These structural features are in stark contrast to the branch morphologies in synthetic cellular solids produced through the standard foaming process. The cross-section of the branches in these foams is characterized by the form of a three-cusp hypocycloid known as Plateau border [46–49].

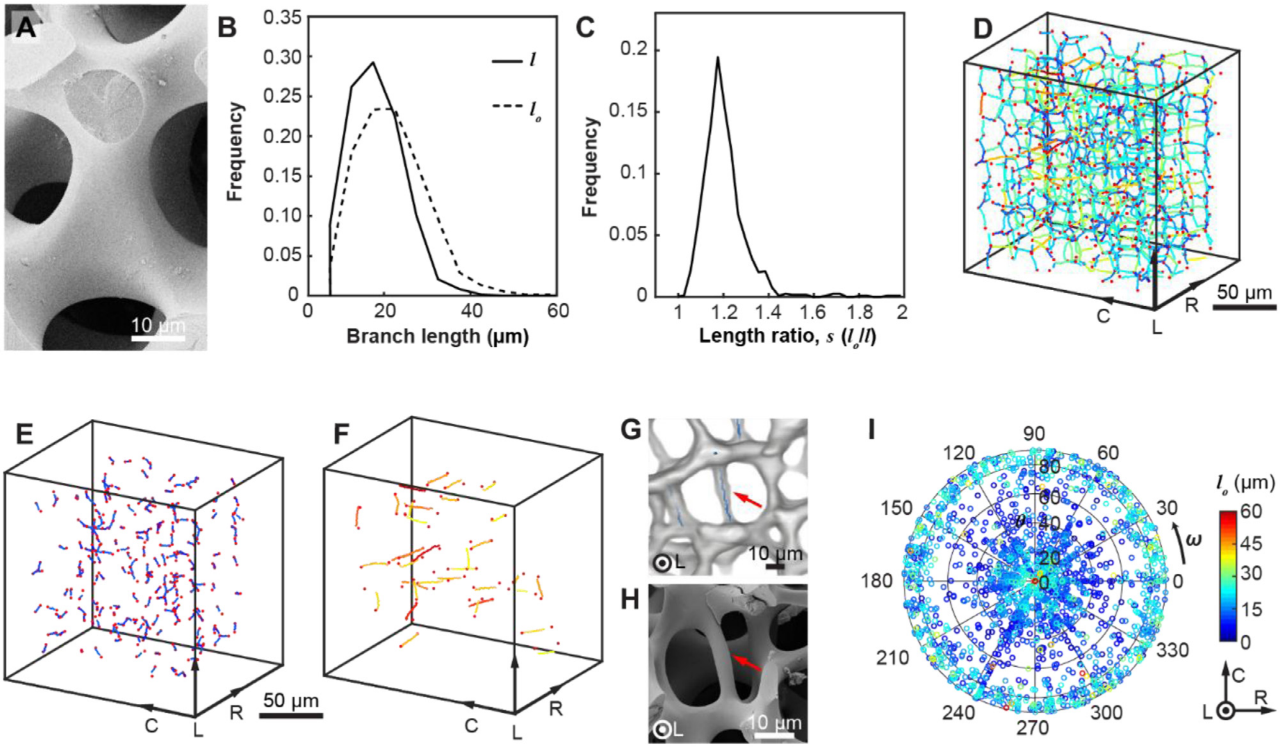

Fig. 7. Quantitative analysis of branch length and orientation. (**A**) SEM image of a representative branch in the sea urchin spine. (**B**) Distribution of branch length l_o and Euclidean distance l. (**C**) Distribution of the length ratio s. (**D**) Network representation of branch length distribution, and corresponding volume (**E**) with branches $< 15.0\,\mu m$ and (**F**) with branches $> 40.0\,\mu m$. (**G**) 3D rendering and (**H**) SEM image of representative examples of long branches as indicated in (**F**). (**I**) Correlation of branch orientation and length. (**D-F**) are based on the same color scale as in (**I**).

3.4. Local cellular level: ring characteristics

The ring detection algorithm is used to study the local branch organization characteristics. Fig. 9A depicts four examples of detected ring structures with different ring types and the corresponding 3D renderings. As shown in Fig. 9B, the complete ring detection in this representative volume can be achieved, which can be labeled and mapped to the cellular skeleton. This volume contains 213 4-B rings, 577 5-B rings, 614 6-B rings, and 476 7-B rings (Fig. 9C). All the ring types seem to distribute uniformly within this volume. The diameters of the 4-B, 5-B, 6-B, and 7-B rings are $23.1 \pm 5.8\,\mu m, 28.2 \pm 13.6\,\mu m, 30.4 \pm 5.0\,\mu m$, and $34.7 \pm 7.0\,\mu m$, respectively (Fig. 9D). This indicates that the ring size increases with the number of branches contained in a ring. The measured average diameter of all rings is $30.0 \pm 9.6\,\mu m$ ($N = 1880$). The ring size obtained here is broadly consistent with the pore diameter measurement based on 2D measurement of fully-grown *H. mamillatus* spines [25]. Lastly, our algorithm allows for determining the orientation of these rings. As shown in Fig. 9E, most of the detected rings, regardless of their ring types, are aligned perpendicular to the *R*-*C* plane.

3.5. Global network level: chain alignment

We investigate the branch alignment by detecting "branch chains" and evaluating the misorientations among adjacent branches as well as with respect to a global reference orientation. As shown in Figs. 6A and 10A, the branches in this location appear to have preferred alignments in the *L* direction. Our algorithm successfully detected these branch chains aligned in this direction (total number of detected chains = 62, Fig. 10B). From the top view of the same volume, these branch chains appear to form a Voronoi-like pattern, which may be a result of the biomineralization formation process along the *L* direction in this region [50] (Fig. 10C). The misorientation angle φ with respect to the *L* direction ranges from 0 to 50°, while the inter-branch angle β between adjacent branches are $90^\circ - 180^\circ$ The length and thickness of the branches in these chains are $19.0 \pm 6.5\mu$m and $6.8 \pm 1.2\mu$m ($N = 957$), respectively (Fig. 10E and F), which are shorter and thicker compared to the mean branch length and thickness of the whole volume, respectively. The preferred alignment of branches along the *L* direction with shorter and thicker branches revealed here is expected to have a significant impact on the anisotropy of the mechanical properties, which will lead to enhanced resistance to withstand loads in the *L* direction.

3.6. Global network level: 3D-FFT analysis

On the global network level, we also utilize the 3D-FFT analysis to investigate the long-range organization characteristics of the cellular network. A larger region ($530\,\mu m(R) \times 500\ \mu m(C) \times 500\,\mu m(L)$) in a similar location was used for this analysis. The same skeletonization and network cleaning procedures were first applied to obtain the skeletonized network, which consists of 11,540 nodes and 21,049 branches (Fig. 11A, B). The 3D-FFT analysis was performed on the node array of the skeletonized network. As shown in Fig. 11C, localized high-intensity Fourier peaks in multiple directions with different periodicity are observed, which demonstrates large scale orderliness of the cellular network. Visualizing the FFT pattern in the L-C plane, the first-order Fourier peak in the *L* direction is at 0.034 μm^{-1} away from the origin (d_1), corresponding to the diameter of the ring structures (~30μm) aligned in this direction (Fig. 11D). The second-order peak appears at 0.068 μm^{-1} (d_2), corresponding to the average branch length detected in the chain structures in this direction (~15μm). In the *R*-*C* plane,

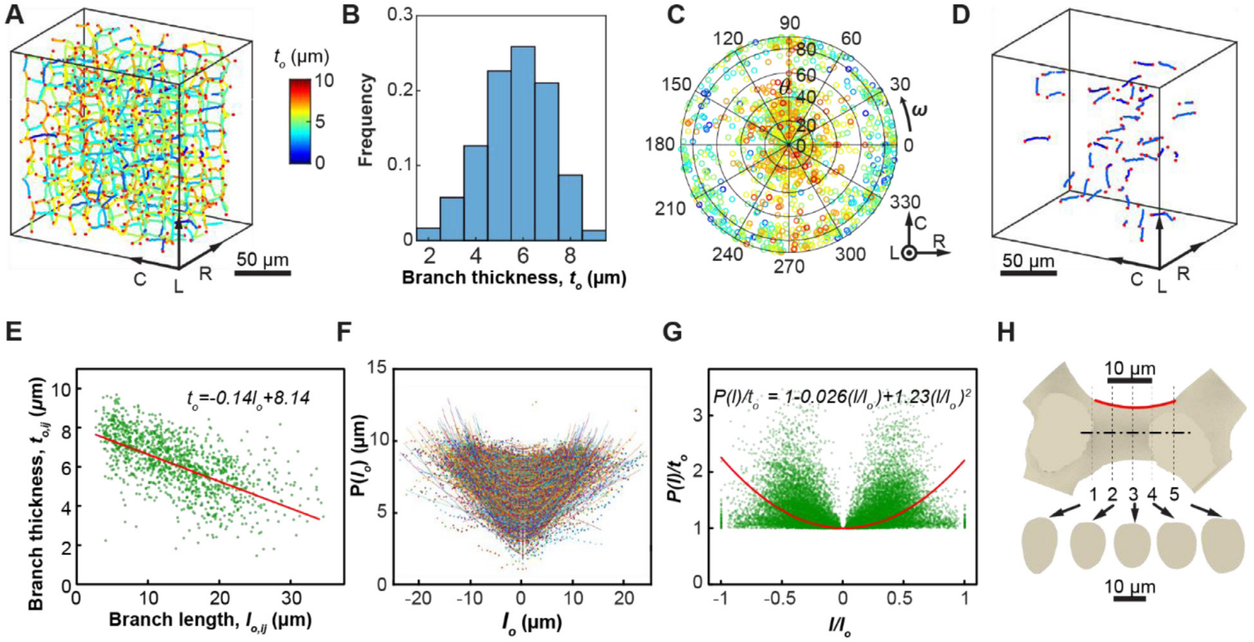

Fig. 8. Quantitative analysis of branch thickness, orientation, and morphology. (**A**) Network representation of branch thicknesses (t_o). (**B**) Statistical distribution of branch thicknesses t_o in the analyzed volume. (**C**) Correlation between branch orientation and thickness. (**D**) Distribution of branches with thickness $t_o < 3.3\,\mu m$. Note that (**A, C, D**) are based on the same color scale for branch thickness. (**E**) Correlation between branch length and thickness. (**F**) Measurements of branch profiles and the fitting results for individual branches in this volume. (**G**) Normalized branch profiles of all branches and the fitting result (red line). (**H**) 3D volume rendering of a representative branch, overlapped with the fitting result in the red line. Five cross-sectional slices of this branch in different positions are displayed.

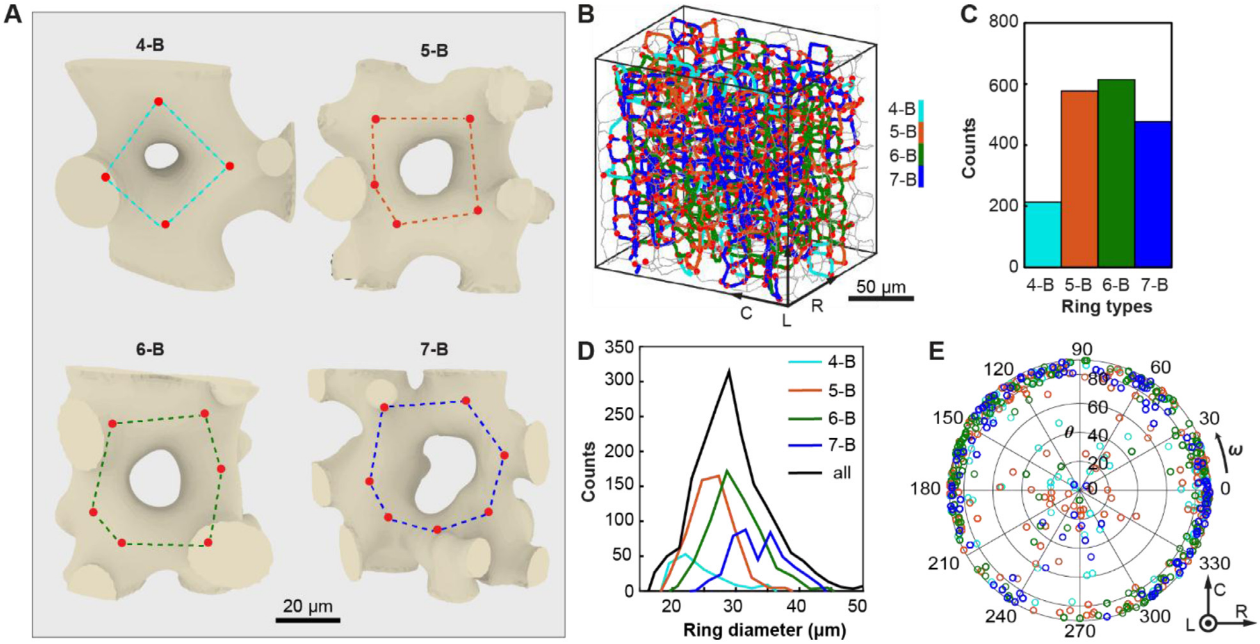

Fig. 9. Analysis of ring structures. (**A**) 3D rendering of different ring types overlaid with registered nodes and connected branches. (**B**) Ring structures detected and labeled according to their ring types in the analyzed volume. (**C**) Distribution of ring types. (**D**) Distribution of ring diameter for different ring types and all rings detected in this volume. (**F**) Correlation between ring types and orientation. Note the color scheme is used consistently for different node types in this figure.

the circular distribution of high-intensity region is observed at $0.022 - 0.052\ \mu\text{m}^{-1}$, which matches well with the branch length distribution (19-45 μm) in this plane (Fig. 11E). The circular peaks also indicate random distributions of branches in the *R-C* plane, consistent with the result shown in Fig. 7I.

4. Discussions

In this work, we introduced a computational tomography data analysis pipeline for investigating the 3D structure of natural porous materials, particularly the stereom structure for echinoderms. By using sea urchin spines as a model system, we systematically presented the development and capability of this multi-step methodology. For the preprocessing steps related to reconstruction and segmentation of tomography data, we developed a hierarchical CNN-based method by taking advantage of the inherent structural characteristics of the stereom structure exhibited at multiple length scales. We demonstrated that this approach not only can greatly minimize noises and artifacts but also allow for efficient compressive sensing compared to conventional reconstruction and

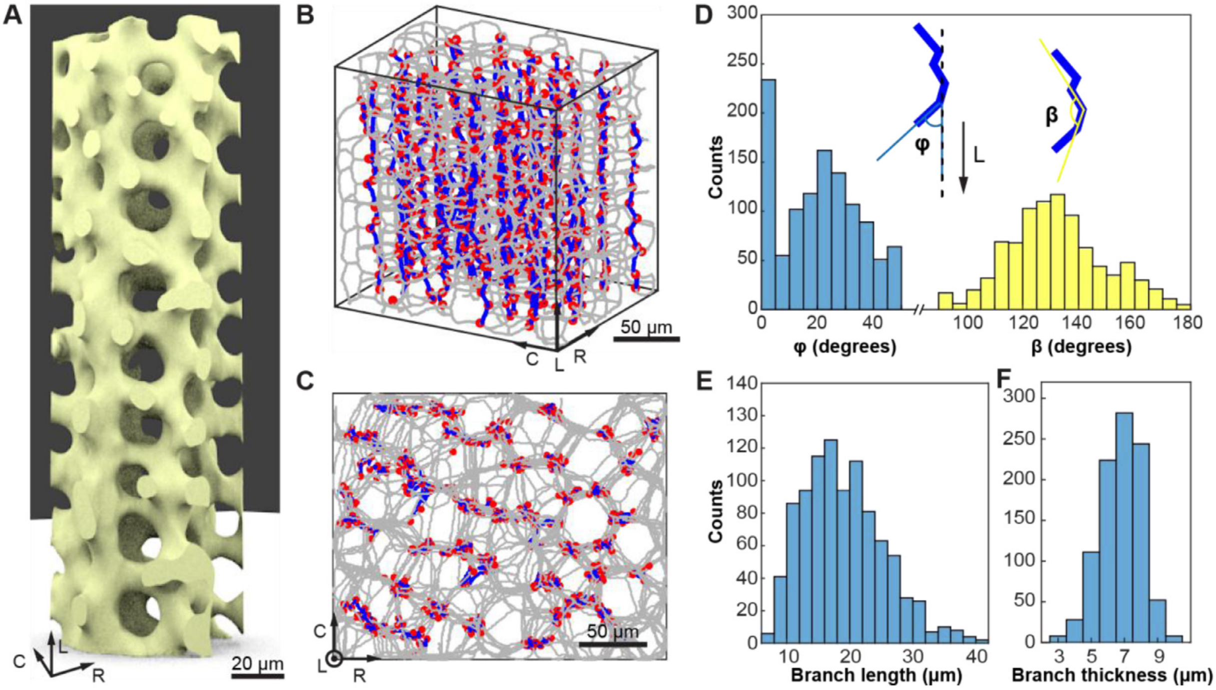

Fig. 10. Analysis of chain structures. (**A**) 3D rendering of the cellular structure observed in the analyzed region close to the center of the sea urchin spines, from which the longitudinal alignment of branches can be qualitatively observed. (**B, C**) Detected branch chains along the longitudinal direction viewed (**B**) from the side and (**C**) from the R-C plane. (**D**) Distributions of the misorientation angles between a branch and the L direction (φ) and inter-branch angles between two adjacent branches (β) in the chain structures. Distribution of (**E**) branch length and (**F**) thickness for the branches in the detected chains in (**B**).

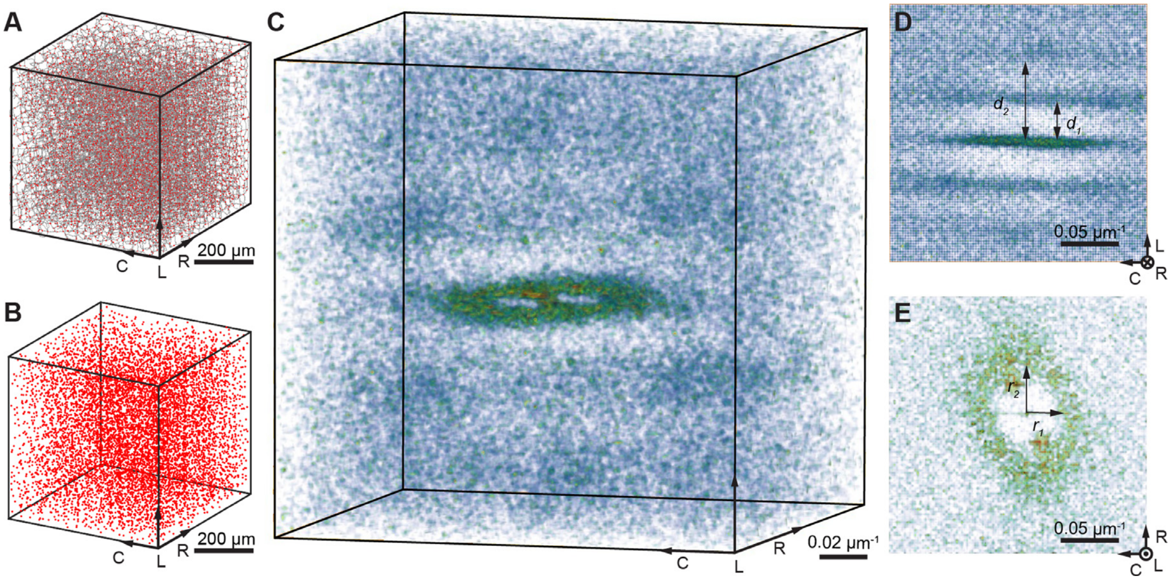

Fig. 11. 3D-FFT analysis of nodes in the cellular network. (**A**) Skeletonized network and (**B**) corresponding node distribution of the selected volume. (**C-E**) Volumetric rendering of the 3D-FFT analysis of the volume shown in (**B**), shown in (**C**) side view, (**D**) view in the L-C plane, and (**E**) view in the R-C plane.

segmentation approaches. In terms of the network construction and registration, although the iterative erosion method is standard and widely used for skeletonization, post-processing is required, especially for the complex 3D porous structures like stereom. Our iterative, adaptive trimming and merging treatments are essential to achieve a clean and reliable cellular network. This step is crucial for robustly analyzing structural descriptors later and for providing a reliable network model for mechanical modeling, as shown in the second paper of this work series [29]. For the feature extraction and analysis step, we developed a series of descriptors to quantify the structural features at three different length scales, including 1) node type, inter-branch angle, node orientation and planarity, branch length, distance, length ratio, thickness, orientation, and profile at individual node and branch level, 2) ring number, orientation, and size at local cellular level, and 3) branch chain and long-range orderliness based on 3D-FFT analysis at global network level. This multiscale structural information for the 3D network organization can provide important insights for the understanding of the mechanical designs of biological cellular solids. In addition, as shown in Supplementary Information, the pipeline introduced here can be easily tailored to analyzing 3D printed lattice-like structures, providing an efficient tool for mechanical modeling and quality control of these structures.

Within the analysis volume, the porous stereom structure of sea urchin spines is primarily constructed with N-3 and N-4 nodes. A recent study revealed that the porous trabecular bone is also dominated by similar low-connectivity nodes [4]. The underlying principles for the formation of such low-connectivity nodes in these natural systems are currently unclear. Regarding their mechanical implications, it is known that low-connectivity nodes tend to result in bending dominated lattice structures, which is generally considered less effective compared to stretch dominated structures [2,51]. Further study is required to better elucidate the mechanical roles of this design strategy. In addition, similar to trabecular bone, the inter-branch angles for N-3 and N-4 nodes are very close to the values for the idealized triangle and tetrahedron structures [4]. This suggests that the branches connected to a common node tend to maximize the 3D space in stereom, similar to trabecular bone. As proposed by the previous study, such structural design may be beneficial to resist multidirectional loading [4].

The combined analysis results indicate the mechanical anisotropy of stereom structures can be controlled via a number of ways. First, branches can form preferred orientational alignment as revealed by our branch chain analysis. Such a strategy follows the concept of Wolff's law, which suggested that the human femur may be strengthened in specific loading directions through the preferred alignment of individual trabeculae [52]. Moreover, thanks to this branch chain analysis, we directly demonstrated that branches along these chains are thicker and shorter compared to the average values. This will further enhance the structural stiffness and strength in the alignment direction, *i.e.*, the L direction. Here we note that this preferred alignment along the longitudinal direction should be closely related to the fact that the analysis volumes are near the center region of the sea urchin spines. Such alignment may be directly affected by the microscopic biomineralization process, as a number of previous studies have shown that the stereom formation in the center region of spines initiates from the branches along the longitudinal direction [50,53,54]. The Voronoi-like organization of branch chains in the transverse cross section may be also closely related to this process. As shown in the second study of this work series based on the large-scale analysis, such structural alignment exhibits gradual local variations, leading to gradient mechanical properties within sea urchin spines [29].

Despite relatively small analysis volumes, our results reveal a number of important differences between sea urchin spines' stereom structure and synthetic open-cell foams fabricated through conventional foaming processes [2,55]. First of all, most branches in the analysis volume are highly curved. The thickness profile can be fitted with a second-order polynomial. In contrast, the branches in synthetic foams produced through standard foaming processes often exhibit large portions with relatively constant thickness [46–49]. We also note that some long branches (length > 40 µm) in stereom exhibit relatively constant thickness over a long distance (Fig. 7G and H). These branches appear to be reinforcing structures for the large holes in the Voronoi-like patterns in the R-C plane. Second, the cross sections of stereom's branches are generally circular, whereas in synthetic foams, the branches exhibit a three-cusp hypocycloid known as Plateau border during the foaming process [46–49]. Third, our ring analysis indicates that 5-B and 6-B rings are dominating types in stereom, and the average number of branches per ring is estimated to be 5.7. This value is higher compared to that for synthetic foams with random polyhedral cell geometries (~5.1), which is governed by the well-known Euler's law [2,56–59]. The difference revealed here is believed due to the difference in underlying formation mechanisms of the stereom's porous structure and synthetic foams.

Increasing interests have been recently directed to mimicking the "biological forms" of cellular solids in engineering material systems to improve their mechanical performance [60,61]. In particular, 3D printing has been demonstrated as an effective approach for fabricating cellular solids with structural precision down to individual branch level [62–64]. 3D printing allows for the production of cellular structures not bounded by the physical constraints in the conventional synthetic foaming processes [2,55]. However, most of the current 3D-printed cellular materials are based on periodic tessellations of unit cells with idealized geometries, such as cylindrical beams with a constant cross-sectional area. These structures at both local and global scales are still far more simplified and less controlled compared to biological cellular structures. In this regard, the methodology introduced here holds great potential in providing important insights for improved "mimicking" of the natural cellular structures via quantitative analysis of these materials in 3D.

5. Conclusion

In summary, we present a computational tomography analysis pipeline for multiscale structural representation and quantification of biological cellular materials by using sea urchin spines as an example. At the individual branch and node level, this methodology allows for the quantification of a series of structural parameters, such as node type, inter-branch angle, orientation and planarity of nodes, branch orientation, length, thickness, and branch morphology profile. The analysis indicates that the porous structure of sea urchin spines is primarily composed of three- and four-branched nodes, which resemble ideal branched structures that span 3D space maximally. The thickness and length of branches are highly correlated with their orientation, where shorter and thicker branches are aligned with the longitudinal direction of the spines in the analyzed regions. The algorithm is able to extract the morphology profiles of individual branches, from which the highly curved branches can be fitted with a parabolic function, significantly different from synthetic foams. At the local cellular level, the algorithm allows for the investigation of the interconnections and alignments of adjacent branches by detecting branch rings and chains. 3D-FFT analysis of registered nodes over large 3D volumes is developed. The analysis results suggest that the cellular structure has a well-controlled alignment along the longitudinal direction while maintaining a relatively isotropic organization in the transverse direction. We expect that this algorithm can be utilized to conduct the structural analysis of a variety of synthetic or biological cellular solids, such as other echinoderms' stereom structures, enabling quantitative comparative investigation. Further insights in understanding the structure-property of the biological cellular materials such as sea urchin spines enabled by this study could lead to the development of bio-inspired lightweight structures with structural controls at multiple length scales.

Declaration of Competing Interest

The authors declare that they have no known competing financial interests or personal relationships that could have appeared to influence the work reported in this paper.

Acknowledgments

We gratefully acknowledge the National Science Foundation under award number CMMI-1825646. This research used resources of the Advanced Photon Source, a U.S. Department of Energy (DOE)

Office of Science User Facility operated for the DOE Office of Science by Argonne National Laboratory under Contract No. DE-AC02-06CH11357. L.L. also thanks the Department of Mechanical Engineering at Virginia Tech for the support. We thank Dr. X. Xiao, Dr. P. D. Shevchenko, and Dr. F. De Carlo for their technical assistance with synchrotron measurement.

Author contributions

T.Y. performed synchrotron experiments and electron microscopy measurements. T.Y., Z.W., and H.C. developed the cellular network analysis algorithm. T.Y. and Z.W. prepared figures, tables, and wrote the draft manuscript. All authors interpreted results. L.L. designed the research, and L.L. and Y.Z. supervised the project.

Supplementary materials

Supplementary material associated with this article can be found, in the online version, at doi:10.1016/j.actbio.2020.02.034.

References

[1] L. Gibson, M. Ashby, B. Harly, Cellular Materials in Nature and Medicine, Cambridge University Press, 2010.

[2] L.J. Gibson, M.F. Ashby, Cellular Solids Structure and Properties, Cambridge University Press, 1999.

[3] N. Reznikov, R. Shahar, S. Weiner, Three-dimensional structure of human lamellar bone: the presence of two different materials and new insights into the hierarchical organization, Bone 59 (2014) 93–104.

[4] N. Reznikov, H. Chase, Y. Ben Zvi, V. Tarle, M. Singer, V. Brumfeld, R. Sharhar, S. Weiner, Inter-trabecular angle: a parameter of trabecular bone architecture in the human proximal femur that reveals underlying topological motifs, Acta Biomater. 44 (2016) 65–72.

[5] G. Donnay, D.L. Pawson, W.L. Sjogren, G. Donnay, D.L. Pawson, W.L. Sjogren, X-ray diffraction studies of echinoderm plates, Science 166 (1969) 1147–1150.

[6] J.N. Grossmann, J.H. Nebelsick, Comparative morphological and structural analysis of selected cidaroid and camarodont sea urchin spines, Zoomorphology 132 (2013) 301–315.

[7] K.M. Wilbur, Mineral regeneration in echinoderms and molluscs, Cubaa Found Symp. 11 (1973) 7–33.

[8] J. Aizenberg, J.C. Weaver, M.S. Thanawala, V.C. Sundar, D.E. Morse, P. Fratzl, Skeleton of euplectella sp.: structural hierarchy from the nanoscale to the macroscale, Science 309 (2005) 275–278.

[9] N. Tsafnat, J.D. Fitz Gerald, H.N. Le, Z.H. Stachurski, Micromechanics of sea urchin spines, PLoS ONE 7 (2012) e44140.

[10] V. Presser, C. Kohler, Z. Živcová, C. Berthold, K.G. Nickel, S. Schultheiß, E. Gregorová, W. Pabst, Sea urchin spines as a model-system for permeable, light-weight ceramics with graceful failure behavior. part II. mechanical behavior of sea urchin spine inspired porous aluminum oxide ceramics under compression, J. Bionic Eng. 6 (4) (2009) 357–364.

[11] J.C. Weaver, J. Aizenberg, G.E. Fantner, D. Kisailus, A. Woesz, P. Allen, K. Fields, M.J. Porter, Frank W.Zok, P.K. Hansma, P. Fratzl, D.E. Morse, Hierarchical assembly of the siliceous skeletal lattice of the hexactinellid sponge euplectella aspergillum, J. Struct. Biol. 158 (1) (2007) 93–106.

[12] V. Presser, S. Schultheiß, C. Berthold, K.G. Nickel, Sea urchin spines as a model-system for permeable, light-weight ceramics with graceful failure behavior. part I. mechanical behavior of sea urchin spines under compression, J. Bionic Eng. 6 (3) (2009) 203–213.

[13] H.A. Lowenstam, S. Weiner, On Biomineralization, Oxford University Press, 1989.

[14] A.B. Smith, Stereom microstructure of the echinoid test, Special Pap. Palaeontol. 25 (1980) 1–81.

[15] J.N. Weber, The incorporation of magnesium into the skeletal calcites of echinoderms, Am. J. Sci. 267 (5) (1969) 537–566.

[16] J. Seto, Y. Ma, S.A. Davis, F. Meldrum, A. Gourrier, Y.-.Y. Kim, U. Schilde, M. Sztuckig, M. Burghammerg, S. Maltsevi, C. Jägeri, H. Cölfena, Structure-property relationships of a biological mesocrystal in the adult sea urchin spine, Proc. Natl. Acad. Sci. U. S. A. 109 (10) (2012) 3699–3704.

[17] C. Moureaux, A. Pérez-Huerta, P. Compère, W. Zhu, T. Leloup, M. Cusack, P. Dubois, Structure, composition and mechanical relations to function in sea urchin spine, J. Struct. Biol. 170 (1) (2010) 41–49.

[18] J.N. Weber, Origin of concentric banding in the spines of the tropical echinoid heterocentrotus, Pacific Sci. 23 (4) (1969) 452–466.

[19] T. Chen, Microstructure and micromechanics of the sea urchin, colobocentrotus atratus, Massachsetts Institute of Technology, 2011.

[20] M. Lai, A.N. Kulak, D. Law, Z. Zhang, F.C. Meldrum, D.J. Riley, Profiting from nature: macroporous copper with superior mechanical properties, Chem. Commun. 1 (34) (2007) 3547–3549.

[21] H.U. Nissen, Crystal orientation and plate structure in echinoid skeletal units, Science 166 (1969) 1150–1152.

[22] M. Jensen, The ultrastructure of the echinoid skeleton, Sarsia 48 (1972) 39–48.

[23] E. Merker, Studien am skelet der echinodermen, Zool. Jabrb. Abt. Allg. Zool. Physiol. Tiere 36 (1916) 25–205.

[24] F. Deutler, Über das wachstum des seeigelskeletts, Zool. Jabrb. Abt. Anat. Ontog. Tiere 48 (1926) 119–200.

[25] J.N. Großmann, Stereom Differentiation in Sea Urchin Spines Under Special Consideration As a Model For a New Impact Protective System, Universität Tübingen, 2010.

[26] C. Lauer, T.B. Grun, I. Zutterkirch, R. Jemmali, J.H. Nebelsick, K.G. Nickel, Morphology and porosity of the spines of the sea urchin heterocentrotus mamillatus and their implications on the mechanical performance, Zoomorphology 137 (1) (2017) 139–154.

[27] V. Presser, K. Gerlach, A. Vohrer, K.G. Nickel, W.F. Dreher, Determination of the elastic modulus of highly porous samples by nanoindentation: a case study on sea urchin spines, J. Mater. Sci. 45 (9) (2010) 2408–2418.

[28] T.B. Grun, J.H. Nebelsick, Structural design of the echinoid's trabecular system, PLoS ONE 13 (2018) 1–18.

[29] T.Yang H.Chen, Z. Wu, Z. Deng, Y. Zhu, L. Li, Quantitative 3D structural analysis of the cellular microstructure of sea urchin spines (II): large-volume structural analysis, Acta Biomater. (2020) In press.

[30] J. Schindelin, J. Schindelin, I. Arganda-Carreras, E. Frise, V. Kaynig, M. Longair, T. Pietzsch, S. Preibisch, C. Rueden, S. Saalfeld, B. Schmid, J.-.Y. Tinevez, D.J. White, V. Hartenstein, K. Eliceiri, P. Tomancak, A. Cardona, Fiji: an open-source platform for biological-image analysis, Nat. Methods 9 (7) (2012) 676–682.

[31] B. Dowd, G.H. Campbell, R.B. Marr, V. Nagarkar, S. Tipnis, L. Axe, D.P. Siddons, Developments in synchrotron x-ray computed microtomography at the national synchrotron light source, Proc. SPIE 3772 (1999) 224–236.

[32] D. Gürsoy, F. De Carlo, X. Xiao, C. Jacobsen, TomoPy: a framework for the analysis of synchrotron tomographic data, J. Synchrotron Radiat 21 (5) (2014) 1188–1193.

[33] Z. Wu, T. Yang, Y. Zhu, L. Li, Feature-based sparse angle tomography reconstruction for dynamic characterization of bio-cellular materials, Comput. Imaging III 10669 (2018) O1–O8.

[34] B. Münch, P. Trtik, F. Marone, M. Stampanoni, Stripe and ring artifact removal with combined wavelet-Fourier filtering, EMPA Act. 17 (2009) 34–35.

[35] E.X. Miqueles, J. Rinkel, F. O'Dowd, J.S.V Bermúdez, Generalized titarenko's algorithm for ring artefacts reduction, J. Synchrotron Radiat. 21 (6) (2014) 1333–1346.

[36] R. Fitzgerald, Phase-Sensitive X-Ray imaging, Phys. Today 53 (2000) 23–26.

[37] Y. Zhu, G. Barbastathis, Simultaneous phase and absorption imaging in the x-ray band using illumination structured by a single transmission grid, Imaging Appl. Opt. 0 (1) (2015) 4–6.

[38] D. Paganin, S.C. Mayo, T.E. Gureyev, P.R. Miller, S.W. Wilkins, Simultaneous phase and amplitude extraction from a single defocused image of a homogeneous object, J. Microsc. 206 (1) (2002) 33–40.

[39] Z. Wu, X. Li, Y. Zhu, Texture orientation-resolving imaging with structure illumination, Proc. SPIE. 10222 (2017) 0M1-6.

[40] Y. Zhu, Absorption-phase duality in structured illumination transport of intensity (TIE) phase imaging, Proc SPIE 984709 (2016) 1–7.

[41] S. Berg, D. Kutra, T. Kroeger, C.N. Straehle, B.X. Kausler, C. Haubold, M. Schiegg, J. Ales, T. Beier, M. Rudy, K. Eren, J.I. Cervantes, B. Xu, F. Beuttenmueller, A. Wolny, C. Zhang, U. Koethe, F.A. Hamprecht, A. Kreshuk, ilastik: interactive machine learning for (bio) image analysis, Nat Methods 16 (2017) 1226–1232.

[42] Z. Wu, A. Alorf, T. Yang, L. Li, and Y. Zhu, Robust X-ray sparse-view phase tomography via hierarchical synthesis convolutional neural networks, arXiv preprint arXiv:1901.10644 (2019).

[43] H. Homann, Implementation of a 3D thinning algorithm, Insight-J. 421 (2007) 4–7.

[44] P.K. Saha, G. Borgefors, G. Sanniti di Baja, A survey on skeletonization algorithms and their applications, Pattern Recognit. Lett. 76 (2016) 3–12.

[45] Y. Ben-Zvi, N. Reznikov, R. Shahar, S. Weiner, 3D Architecture of trabecular bone in the pig mandible and femur: inter-Trabecular angle distributions, Front. Mater. 4 (2017) 1–15.

[46] A. Liebscher, C. Redenbach, Statistical analysis of the local strut thickness of open cell foams, Image Anal. Stereol. 32 (2013) 1–12.

[47] P. De Jaeger, C. T'Joen, H. Huisseune, B. Ameel, M. De Paepe, An experimentally validated and parameterized periodic unit-cell reconstruction of open-cell foams, J. Appl. Phys. 109 (10) (2011) 1–10.

[48] W.Y. Jang, S. Kyriakides, A.M. Kraynik, On the compressive strength of open–cell metal foams with kelvin and random cell structures, Int. J. Solids Struct. 47 (21) (2010) 2872–2883.

[49] W. Jang, A.M. Kraynik, S. Kyriakides, On the microstructure of open-cell foams and its effect on elastic properties, Int. J. Solids Struct. 45 (2008) 1845–1875.

[50] P. Gorzelak, J. Stolarski, P. Dubois, C. Kopp, A. Meibom, 26Mg labeling of the sea urchin regenerating spine: insights into echinoderm biomineralization process, J. Struct. Biol. 176 (1) (2011) 119–126.

[51] V.S. Deshpande, M.F. Ashby, N.A. Fleck, Foam topology: bending *versus* stretching dominated architectures, Acta Mater 49 (6) (2001) 1035–1040.

[52] J. Wolff, Das Gesetz Der Transformation Der Knochen, Verlag von August Hirschwald, Berlin, 1892.

[53] B.M. Heatfield, Growth of calcareous skeleton during regeneration of spines of sea urchin, strongylocentrotus-purpuratus (Stimpson) - Light and scanning electron microscopic study, J. Morphol. 134 (1) (1971) 57–89.

[54] K.M. Wilbur, Mineral regeneration in echinoderms and molluscs, Cuba Found Symp. 1 (1973) 7–33.

[55] M. Scheffler, P. Colombo, C. Ceramics, C. Paolo, Cellular Ceramics: Structure, Manufacturing, Properties and Applications, Wiley, 2005.

[56] L. Euler, Thoughts On the Elements of Bodies, Memoirs of the Prussian Academy of Science, Berlin, 1746.

[57] I. Lakatos, Proofs and Refutations, the Logic of Mathematical Discovery, Cambridge University Press, 1976.

[58] L.R. Meza, S. Das, J.R. Greer, Strong, lightweight, and recoverable three-dimensional ceramic nanolattices, Science 345 (2014) 1322–1326.

[59] H.X. Zhu, N.J. Mills, J.F. Knott, Analysis of the high strain compression of open–cell foams, J. Mech. Phys. Solids 45 (1997) 1875–1904.

[60] N. Toader, W. Sobek, K.G. Nickel, Energy absorption in functionally graded concrete bioinspired by sea urchin spines, J. Bionic Eng. 14 (2) (2017) 369–378.

[61] A. Bührig-Polaczek, C. Fleck, T. Speck, P. Schüler, S.F. Fischer, M. Caliaro, M. Thielen, Biomimetic cellular metals—using hierarchical structuring for energy absorption, Bioinspir. Biomim. 11 (4) (2016) 45002.

[62] D. Jang, L.R. Meza, F. Greer, J.R. Greer, Fabrication and deformation of three-dimensional hollow ceramic nanostructures, Nat. Mater. 12 (2013) 893–898.

[63] L.R. Meza, S. Das, J.R. Greer, Strong, lightweight, and recoverable three-dimensional ceramic nanolattices, Science 345 (2014) 1322–1326.

[64] X. Zheng, W. Smith, J. Jackson, B. Moran, H. Cui, D. Chen, J. Ye, N. Fang, N. Rodriguez, T. Weisgraber, C.M. Spadaccini, Multiscale metallic metamaterials, Nat. Mater. 15 (10) (2016) 1100–1106.